

Supplementary Material for
**Giant Biquadratic Exchange in 2D Magnets and its Role in Stabilizing Ferromagnetism
of NiCl₂ Monolayer**

J. Y. Ni^{1,2*}, X. Y. Li^{1,2*}, D. Amoroso³, X. He⁴, J.S. Feng^{1,5†}, E. J. Kan⁶, S. Picozzi³, and H. J. Xiang^{1,2,7†}

¹*Key Laboratory of Computational Physical Sciences (Ministry of Education), Institute of Computational Physical Sciences, and Department of Physics, Fudan University, Shanghai 200433, P. R. China*

²*Shanghai Qi Zhi Institution, Shanghai 200030, P. R. China*

³*Consiglio Nazionale delle Ricerche CNR-SPIN Via dei Vestini 31, Chieti 66100, Italy*

⁴*Catalan Institute of Nanoscience and Nanotechnology (ICN2), CSIC, BIST, Campus UAB, Bellaterra, Barcelona, 08193, Spain*

⁵*School of Physics and Materials Engineering, Hefei Normal University, Hefei 230601, P. R. China*

⁶*Department of Applied Physics and Institution of Energy and Microstructure, Nanjing University of Science and Technology, Nanjing, Jiangsu 210094, P. R. China*

⁷*Collaborative Innovation Center of Advanced Microstructures, Nanjing 210093, P. R. China*

*These authors contributed equally to this work.

†email: fjs@hfnu.edu.cn

†email: hxiang@fudan.edu.cn

CONTENTS

Section I. Computational details.....	3
Section II. Additional results on bulk NiCl_2	4
Section III. Additional results on monolayer NiX_2	4
1 Relative energies of NiX_2 with different procedures	4
2 LKAG method.....	7
3 Classical spin analysis based on the Fressier method	9
4 Monte-Carlo simulations of monolayer NiX_2	9
5 Additional results on monolayer NiCl_2 and NiBr_2	10
6 Magnetic anisotropic exchange and single ion anisotropy of monolayer NiX_2	11
Section IV. Origin of giant biquadratic exchange interactions in monolayer NiX_2	12
1 Relation between exchange interactions and energies of different spin states.....	12
2 Three-orbital Hubbard model	13
3 Effective hopping interactions in NiX_2	17
Section V. Biquadratic exchange interactions in monolayer CrCl_3 , CrI_3 , CrGeSe_3 and CrSiTe_3	21
Section VI. Additional results on fictitious perovskite NaNiCl_3	21

Section I. Computational details

Our first-principles density functional theory calculations are based on the projector augmented wave (PAW) method [1] encoded in the Vienna *ab initio* simulation package (VASP)[2]. The exchange-correlation functional of the Perdew-Becke-Erzenh (PBE) [3] form is adopted and the plane-wave cutoff energy is set to 500 eV. To properly describe the strong electron correlation in the Ni 3*d* states, the GGA plus on-site repulsion U method [4] (GGA+ U) was employed with the effective U value ($U_{eff} = U - J$) of 4 eV. The main results will not change if other reasonable U (3~8 eV) values are adopted. The structural optimizations are carried out until the forces acting on atoms are smaller than 0.005 eV Å⁻¹. The NiX₂ monolayer adopts the trigonal 1- T CdI₂ structure with the $P\bar{3}m1$ space group [5]. The lateral lattice constant of the NiX₂ monolayer structure optimized with the ferromagnetic state is 3.501(NiCl₂)/3.697(NiBr₂)/3.983(NiI₂) Å. Spin exchange parameters are obtained using the four-state method [6,7], modified four-state mapping method, LKAG method and Machine Learning Method for Constructing Hamiltonian (MLMCH) [8]. By applying machine learning approaches and statistical analyses, MLMCH is able to find out the most important interaction terms among thousands of candidate terms efficiently and correctly. The truncation distances of 2nd and 4th order terms are both set to 20 Bohr. After symmetry analyses, the number of possible nonequivalent parameters (p_{max}) is 172 (including a constant term). The training set and the testing set contain 150 and 50 sets of data, respectively. For four-state method and MLMCH, we use $5 \times 4 \times 1$ supercell of monolayer NiX₂ to extract the related magnetic parameters.

In our parallel tempering Monte Carlo (PTMC) simulations of spin Hamiltonian [9,10] with the PASP package, a $35 \times 35 \times 1$ supercell of the unit cell is adopted for monolayer NiX₂. Similar result was obtained with larger supercells to estimate the magnetic critical temperature. The number of replicas is set to 256.

Section II. Additional results on bulk NiCl_2

For bulk NiCl_2 , we find that the energy of the ferromagnetic state is 0.01 eV higher than that of interlayer antiferromagnetic state, consistently with the literature [see Crystals **7**, 121 (2017); Phys. Rev. Materials **3**, 044001 (2019)]. The inter-layer nearest and next nearest exchange interactions are found to be -0.02 meV and 0.25 meV, respectively. Thus, the inter-layer exchange interactions are much weaker than the intra-layer exchange interactions, suggesting that the inter-layer interactions have negligible effects on the intra-layer spin ordering.

Section III. Additional results on monolayer NiX_2

1 Relative energies of NiX_2 with different procedures

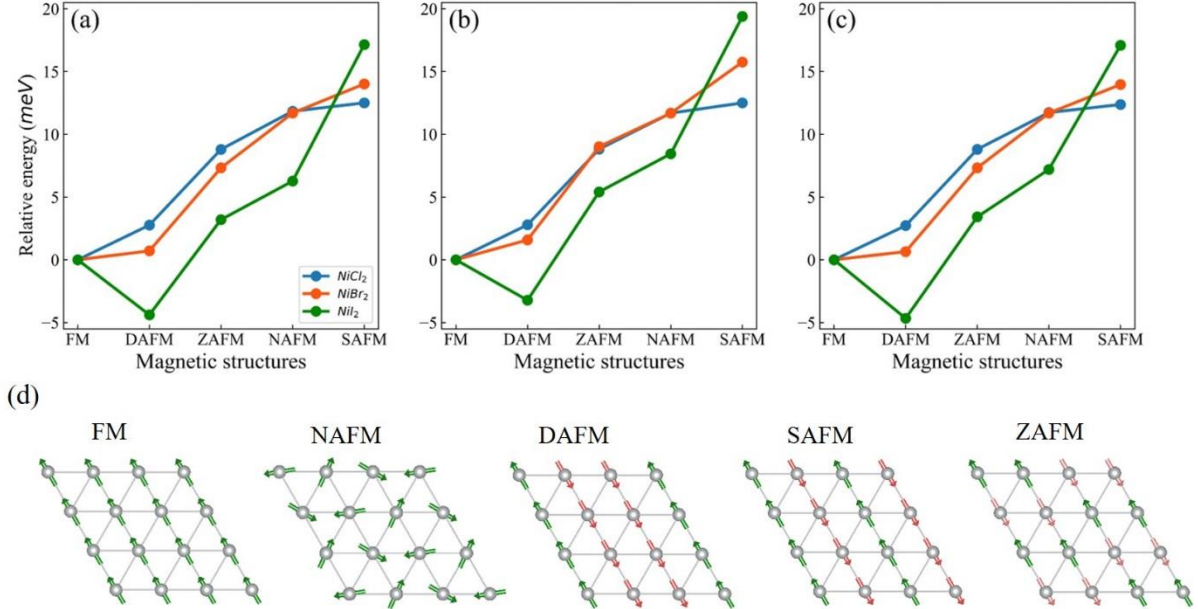


FIG. S1 (a) Calculated relative energies for various commensurate magnetic structures of monolayer NiX_2 by GGA+U method using the structure optimized with the FM order. (b) Relative energies based on GGA+U+SOC calculation using structures optimized with FM order. (c) Relative energies based on GGA+U calculation using structures full optimized with FM, DAFM, ZAFM, NAFM, SAFM spin order, respectively. (d) Schematic top view of various commensurate magnetic structures. Note that $U = 4$ eV is adopted.

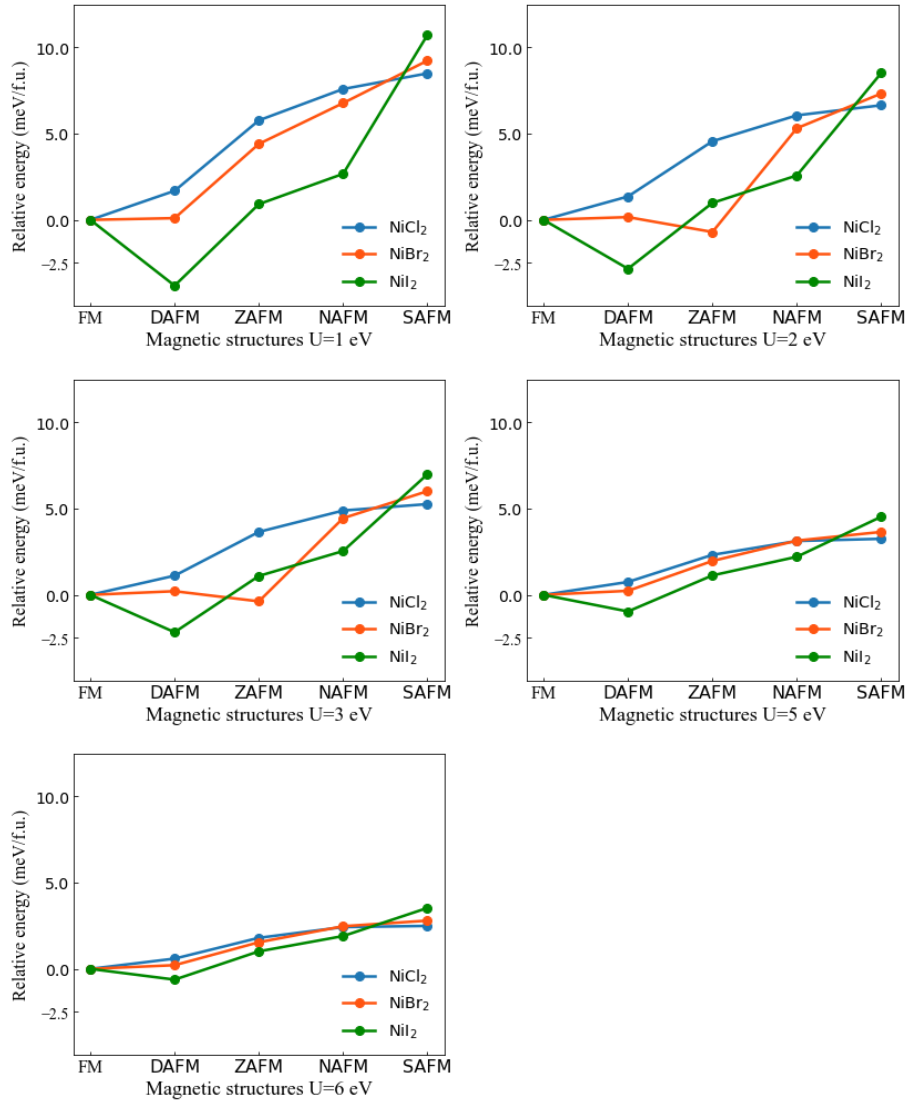
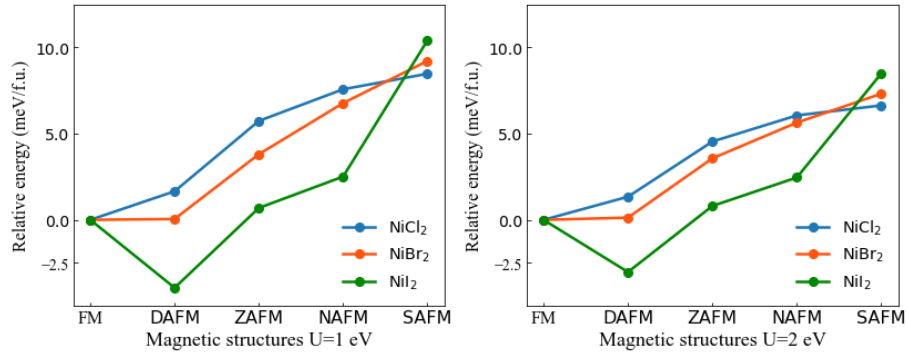


FIG. S2 relative energies for various commensurate magnetic structures of monolayer NiX_2 by GGA+U method using the structure optimized with the FM order by adopting different U values.



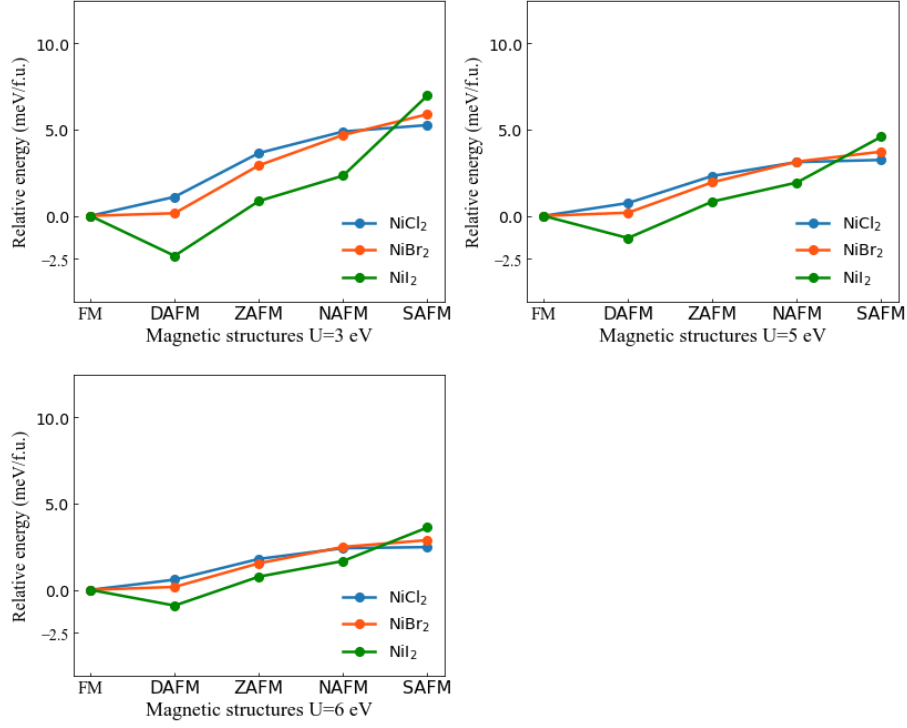
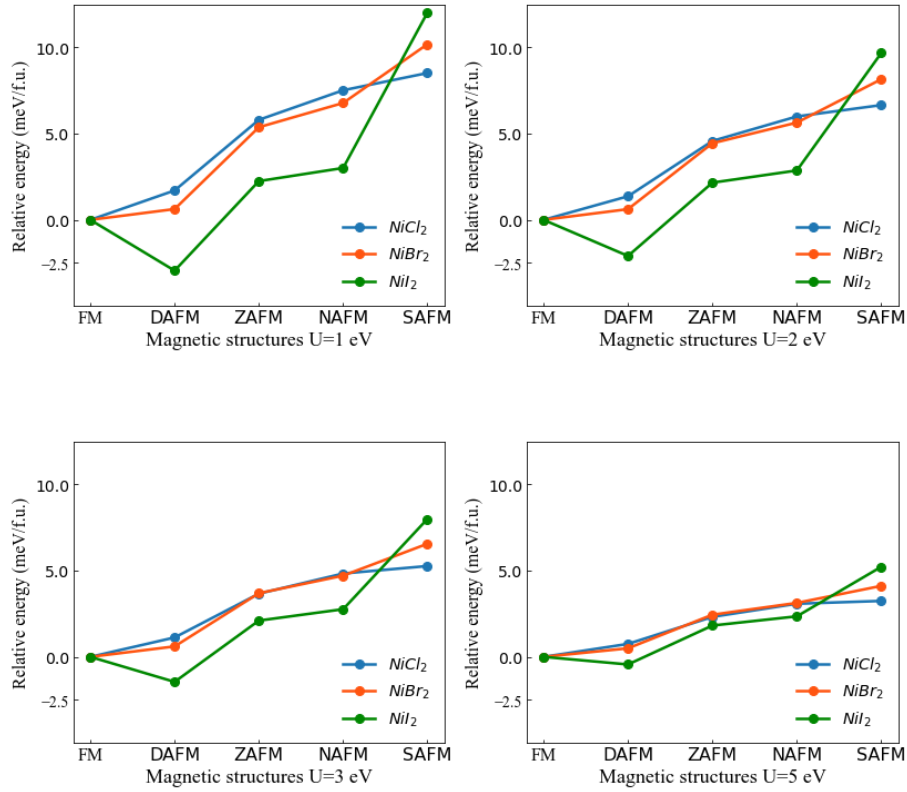


FIG. S3 Relative energies based on GGA+U+SOC calculation using structures optimized with FM order by adopting different U values.



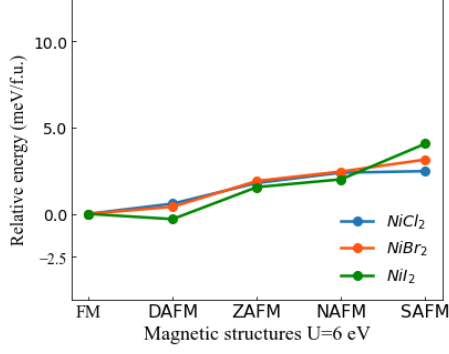


FIG. S4 Relative energies based on GGA+U calculation using structures full optimized with FM, DAFM, ZAFM, NAFM, SAFM spin order by adopting different U values.

2 LKAG method

The process of calculating the exchange interactions of monolayer NiCl₂ based on the LKAG formalism[11] is as follows: we first build the effective tight binding Hamiltonian based on Maximally localized Wannier function (MLWF) with Wannier90 package[12,13], which includes the Ni 3*d* and Cl 2*p* orbitals as initial projectors, then we calculate *J* by perturbing the local spin rotation of the Wannier functions, using the LKAG equation as implemented in the TB2J package[14]:

$$J_{ij} = \frac{1}{2\pi} \text{Im} \int_{-\infty}^{E_F} \text{Tr}_L \Delta_i G_{ij,\downarrow}(\varepsilon) \Delta_j G_{ji,\uparrow}(\varepsilon) d\varepsilon \quad (\text{S.1})$$

Where $G(\varepsilon)$ is the Green function in real space between site *i* and *j* in spin channel σ ; Tr_L means the trace over orbital indices, $\Delta_i = H_{i\uparrow} - H_{i\downarrow}$ and H is the Wannier function tight-binding Hamiltonian. Note that there is a factor of -2 between the conventions of *J* use this work and in Refs[11,14].

In monolayer NiCl₂, we notice that there is a large magnetic moment of about 0.2 μ_B per atom on the ligands, of which the contribution to the exchange can not be neglected. This problem has been recently discussed in Refs [15]and[16]. However, the spin moment is not due to the intra-atomic exchange splitting, but the hybridization with the Ni cations. Thus, the ligand spins should be considered to move faster than the cations, and the cations moves adiabatically. We can first treat the ligand spin as an independent component in a Heisenberg model, and then downfold it to a cation only Heisenberg model. Following

Ref[16], we define the cations and ligand subspace T and L. Thus, the exchange matrix for each wavevector \mathbf{q} , J can be written as block matrices:

$$J^O(\mathbf{q}) = \begin{pmatrix} J_{TT} & J_{TL} \\ J_{LT} & J_{LL} \end{pmatrix} \quad (\text{S.2})$$

The downfolded effective exchange between cations can be written as:

$$J^D(\mathbf{q}) = J_{TT} - J_{TL}J_{LL}^{-1}J_{LT} \quad (\text{S.3})$$

Then $J^D(\mathbf{q})$ is transformed to the real space to get the J^D values in real space.

The original and downfolded exchange parameters included the Ni-Ni 1NN, 2NN and 3NN, and Ni-Cl 1NN interactions (Table. S2). The Ni-Ni 1NN effective J^D from the Ni-Cl interaction, as each 1NN Ni-Ni pair is connected by Ni-Cl interaction bonds with ferromagnetic interactions. The other NN's are less impacted by the Ni-Cl interactions. The Ni-Cl exchange should be quite non-Heisenberg, which explains the strong non-bilinearity of the effective 1NN Ni-Ni exchange.

Table S1 Original (J^O) and downfolded (J^D) exchange parameters of the 1NN, 2NN, 3NN, 4NN, 5NN pairs and the 1NN Ni-Cl pair.

	1NN	2NN	3NN	4NN	5NN	Ni-Cl
J^O (meV)	-0.474	0.001	0.92	0.0036	0.0268	-6.10
J^D (meV)	-4.55	-0.05	0.89	0.0064	0.034	0

The Ni-Ni 1NN effective J^D includes not only the bilinear contribution (J^B), also the biquadratic contributions (K). In the limit of small deviation from the ferromagnetic state, there is:

$$\tilde{J}_{ij} = \frac{d^2[U_{ij}^B(\vec{S}_i \cdot \vec{S}_j) + K(\vec{S}_i \cdot \vec{S}_j)^2]}{d\vec{S}_i d\vec{S}_j} = J_{ij}^B + 2K(\vec{S}_i \cdot \vec{S}_j) \quad (\text{S.4})$$

We could estimate the bilinear and biquadratic contributions to the exchanges by fitting the J^D calculated at various deviations from the ferromagnetic $\sqrt{2} \times \sqrt{2}$ supercell, in which each Ni atoms has two 1NN with the same spin and one with opposite spin. We get $J^B = -2.91$ meV and $K = -0.82$ meV for 1NN in monolayer NiCl₂, which are close to the results calculated by MLMCH and modified four states mapping methods.

3 Classical spin analysis based on the Fressier method

Based on the Fressier method [17], using two dominant exchange interactions (FM J_1 and AFM J_3), the spin interaction energy of an ordered spin state with \mathbf{k} can be written as:

$$E(\mathbf{k}) = J_1 \{ \cos[2\pi k_x] + \cos[2\pi k_y] + \cos[2\pi(k_x + k_y)] \} \\ + J_3 \{ \cos[4\pi k_x] + \cos[4\pi k_y] + \cos[4\pi(k_x + k_y)] \} \quad (\text{S.5})$$

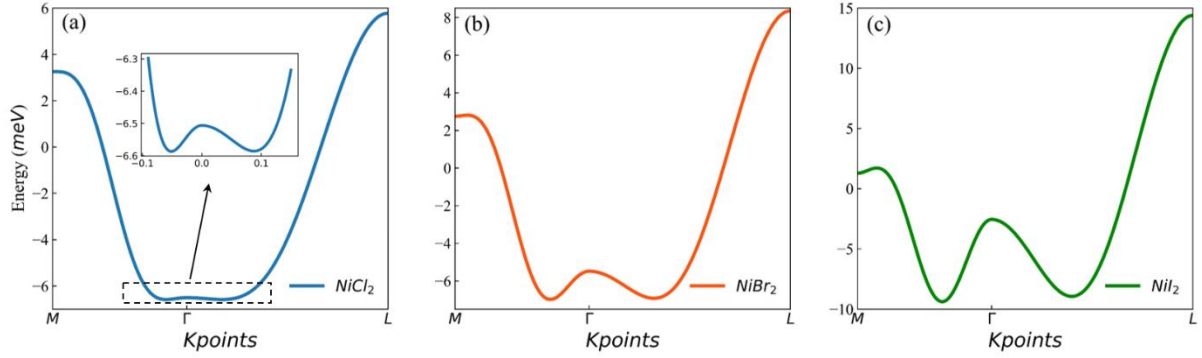


FIG. S5 $E(\mathbf{k})$ vs \mathbf{k} relations along high symmetry lines within the first-Brillouin zone, calculated by Fressier method for monolayer NiCl_2 , NiBr_2 and NiI_2 for (a),(b) and (c) respectively. For monolayer NiCl_2 , minimum of $E(\mathbf{k})$ curve occurs at $\mathbf{k} = (-0.06, 0.12)$. While minimum of $E(\mathbf{k})$ is at $\mathbf{k} = (-0.09, 0.18)$ and $\mathbf{k} = (-0.13, 0.26)$ for monolayer NiBr_2 and monolayer NiI_2 respectively.

4 Monte-Carlo simulations of monolayer NiX_2

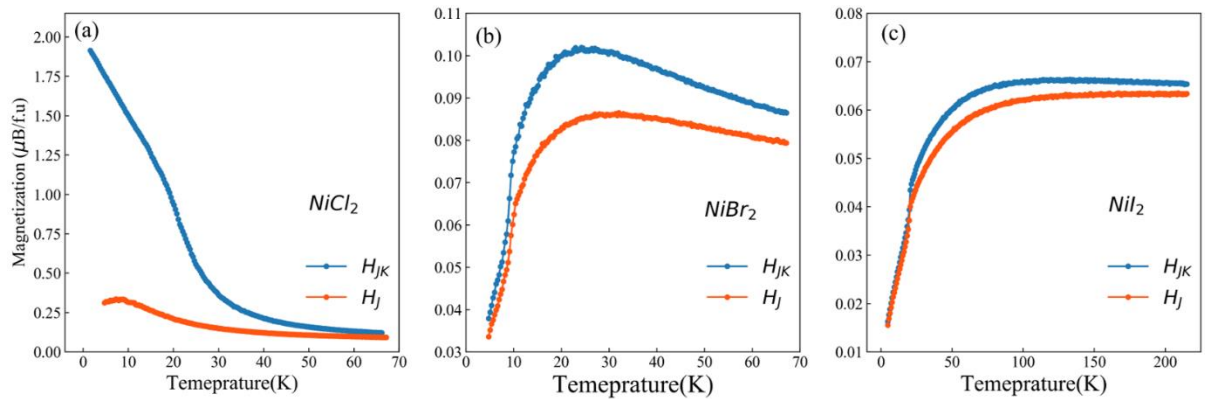


FIG. S6 (a)-(c) The M-T curves obtained by MC simulations based on the Heisenberg model and Heisenberg model plus NN biquadratic interaction, for monolayer NiCl_2 , NiBr_2 and NiI_2 , respectively.

The pure Heisenberg spin Hamiltonian H_J is

$$H_J = \sum_{\langle i,j \rangle} J_1 S_i \cdot S_j + \sum_{\langle i,l \rangle} J_2 S_i \cdot S_l + \sum_{\langle i,k \rangle} J_3 S_i \cdot S_k. \quad (\text{S.6})$$

and the spin Hamiltonian H_{JK} is

$$H_{JK} = \sum_{\langle i,j \rangle} [J_1 S_i \cdot S_j + K(S_i \cdot S_j)^2] + \sum_{\langle i,l \rangle} J_2 S_i \cdot S_l + \sum_{\langle i,k \rangle} J_3 S_i \cdot S_k \quad (\text{S.7})$$

The first, second and last term of right hand of Eq.S.2 and Eq.S.3 represents NN, second-NN, third-NN exchange interaction, respectively.

5 Additional results on monolayer NiCl₂ and NiBr₂

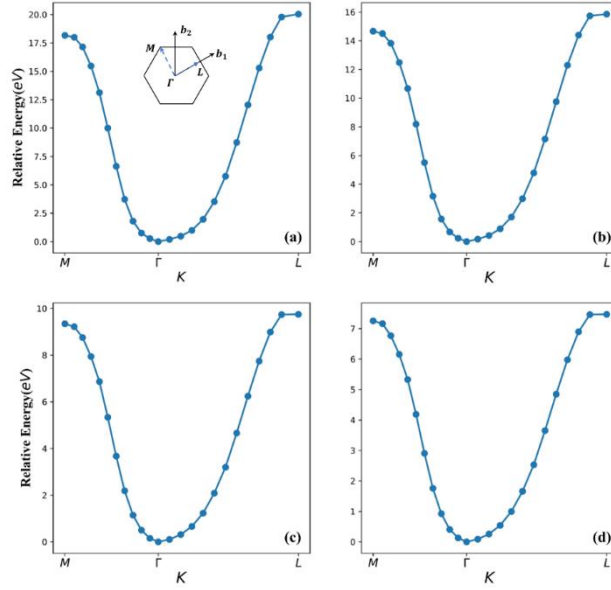


FIG. S7 The relative total-energy dependence of magnetic propagation vector along high symmetry points within the first-Brillouin for monolayer NiCl₂ calculated by different U values. (a) $U = 2\text{eV}$, (b) $U = 3\text{eV}$, (c) $U = 5\text{eV}$, (d) $U = 6\text{eV}$.

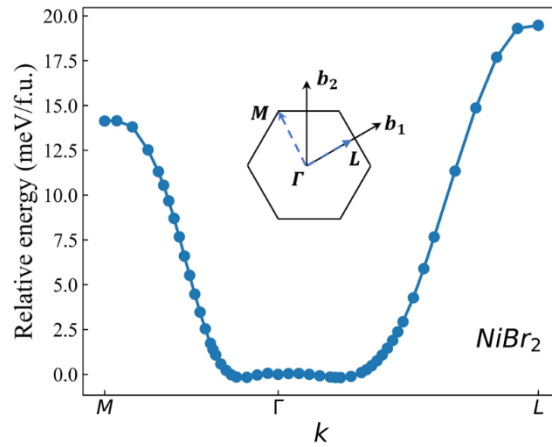


FIG. S8 The dependence of relative DFT total energies on the magnetic propagation vector along high symmetry lines for monolayer NiBr₂.

6 Magnetic anisotropic exchange and single ion anisotropy of monolayer NiX₂

To see the SOC effects on the spin ground state, we employed GGA+U+SOC calculations to extract the magnetic parameters using the $5 \times 4 \times 1$ supercell of monolayer NiX₂ with the four-state method. Since the inversion center exists in the nearest Ni-Ni pairs, the Dzyaloshinskii-Moriya interaction (DMI) arising from SOC is vanishing in monolayer NiX₂. The calculated single ion anisotropies (SIA) and symmetric anisotropic interactions of monolayer NiX₂ are summarized in **Table.S2-3**.

Table S2 Magnetic symmetric anisotropic exchange interactions (J) of the nearest-neighbor Ni-Ni pair and single ion anisotropy coefficient (A_{zz} with $A_{xx} = A_{yy} = 0$) for monolayer NiCl₂, NiBr₂ and NiI₂.

(meV)	J_{xx}	J_{yy}	J_{zz}	J_{xy}	J_{xz}	J_{yz}	A_{zz}
NiCl ₂	-3.101	-3.104	-3.102	-0.0001	0.0002	0.003	0.007
NiBr ₂	-3.832	-3.733	-3.788	0.0004	0.003	-0.07	0.018
NiI ₂	-5.235	-3.835	-4.812	0.001	0.002	-0.84	0.235

Table S3 Magnetic symmetric anisotropic exchange interactions of the third nearest-neighbor Ni-Ni pair for monolayer NiCl₂, NiBr₂ and NiI₂.

(meV)	J_{xx}	J_{yy}	J_{zz}	J_{xy}	J_{xz}	J_{yz}
NiCl ₂	0.912	0.905	0.909	0	0	0
NiBr ₂	1.621	1.599	1.602	0	0	0
NiI ₂	3.425	3.449	3.379	0	0	-0.035

Section IV. Origin of giant biquadratic exchange interactions in monolayer

NiX₂

1 Relation between exchange interactions and energies of different spin states

For each Ni²⁺ ion, there are two holes in the d-shell, resulting in the spin angular moment of 1. For the Ni²⁺-Ni²⁺ pair, the total spin angular moment can be $S=0,1,2$. With the Clebsch-Gordan coefficients, we can construct the state with total spin angular moment S as

$$|S, S_z\rangle = \sum_{S_{1z} S_{2z}} \langle S_1 S_{1z} S_2 S_{2z} | S S_z \rangle |S_1, S_{1z}\rangle |S_2, S_{2z}\rangle.$$

Here, we write out the state $|S, S_z\rangle$ with spin angular moment $S=0,1,2$ explicitly:

For $S = 0$, there is one state with $S_z = 0$:

$$|S, S_z\rangle = |0, 0\rangle = \frac{1}{\sqrt{3}} (|1, -1\rangle |1, 1\rangle - |1, 0\rangle |1, 0\rangle + |1, 1\rangle |1, -1\rangle)$$

For $S = 1$, there are three states with $S_z = -1, 0, 1$:

$$|S, S_z\rangle = |1, -1\rangle = \frac{1}{\sqrt{2}} (-|1, -1\rangle |1, 0\rangle + |1, 0\rangle |1, -1\rangle)$$

$$|S, S_z\rangle = |1, 0\rangle = \frac{1}{\sqrt{2}} (-|1, -1\rangle |1, 1\rangle + |1, 1\rangle |1, -1\rangle)$$

$$|S, S_z\rangle = |1, 1\rangle = \frac{1}{\sqrt{2}} (-|1, 0\rangle |1, 1\rangle + |1, 1\rangle |1, 0\rangle)$$

For $S = 2$, there are five states with $S_z = -2, -1, 0, 1, 2$:

$$|S, S_z\rangle = |2, -2\rangle = |1, -1\rangle |1, -1\rangle$$

$$|S, S_z\rangle = |2, -1\rangle = \frac{1}{\sqrt{2}} (|1, -1\rangle |1, 0\rangle + |1, 0\rangle |1, -1\rangle)$$

$$|S, S_z\rangle = |2, 0\rangle = \frac{1}{\sqrt{6}} (|1, -1\rangle |1, 1\rangle + 2|1, 0\rangle |1, 0\rangle + |1, 1\rangle |1, -1\rangle)$$

$$|S, S_z\rangle = |2, 1\rangle = \frac{1}{\sqrt{2}} (|1, 1\rangle |1, 0\rangle + |1, 0\rangle |1, 1\rangle)$$

$$|S, S_z\rangle = |2, 2\rangle = |1, 1\rangle |1, 1\rangle$$

For two-site Ni-Ni cluster, the low energy effective spin Hamiltonian is $H_{spin} = J(S_1 \cdot S_2) + K(S_1 \cdot S_2)^2$, the energy (E_S) of state S ($S = 0, 1, 2$) can be computed as $E_S = \langle S | H_{spin} | S \rangle$. Thus, $E_0 = -2J + 4K + C$, $E_1 = \langle 1 | H_{spin} | 1 \rangle = -J + K + C$, $E_2 = \langle 2 | H_{spin} | 2 \rangle = J + K + C$, where C is a constant that has nothing to do with spin. Therefore, we can extract the bilinear exchange interaction J and biquadratic exchange interaction K as $J = (E_2 - E_1)/2$, and $K = E_0/3 + E_2/6 - E_1/2$, which is

consistent with the previous result [18].

2 Three-orbital Hubbard model

In order to explore the bilinear and biquadratic exchange interaction of two-site cluster, the Hubbard model is adopted. Each site has three orbitals and is occupied by two electrons. The Hubbard model can be expressed as

$$H = \sum_{\alpha \neq \alpha', \sigma} t_{\alpha\alpha'} (c_{1,\alpha,\sigma}^\dagger c_{2,\alpha',\sigma} + H.c.) + \sum_{i,\sigma} \Delta (c_{i,3,\sigma}^\dagger c_{i,3,\sigma}) + H_D \quad (\text{S.8})$$

where two-body Hamiltonian H_D (i.e., Hubbard operator, including Coulomb repulsion and exchange interactions) is given by:

$$\begin{aligned} H_D = & \sum_{i,\alpha} U_{i,\alpha} (n_{i,\alpha,\uparrow} n_{i,\alpha,\downarrow}) + \sum_{i,\sigma,\alpha < \alpha'} U' (n_{i,\alpha,\sigma} n_{i,\alpha',\sigma} + n_{i,\alpha,\sigma} n_{i,\alpha',\bar{\sigma}}) - \\ & \sum_{i,\alpha,\sigma} J_H (n_{i,\alpha,\sigma} n_{i,\alpha',\sigma}) - \sum_{i,\alpha < \alpha'} J_H (c_{i,\alpha,\uparrow}^\dagger c_{i,\alpha,\downarrow} c_{i,\alpha',\downarrow}^\dagger c_{i,\alpha',\uparrow} + H.c.) - \\ & \sum_{i,\alpha < \alpha'} J_H (c_{i,\alpha,\uparrow}^\dagger c_{i,\alpha',\uparrow} c_{i,\alpha,\downarrow}^\dagger c_{i,\alpha',\downarrow} + H.c.) \end{aligned} \quad (\text{S.9})$$

In Eq.(S.8) and Eq.(S.9), “ i ” represents the site (1 and 2), α/α' stands for the orbital and σ denotes spin angular momentum, U (U') represents Coulomb repulsion between electrons in the same (different) orbitals and J_H (>0) is Coulomb exchange interaction $t_{\alpha\alpha'}$ is inter-site hopping amplitude between orbital α and α' of different site.

To see the dependence of J and K on the hopping amplitude t , besides the case considered in main text, we consider the case in which $t_{11} = t_{12} = t_{13} = t_{33} = 0$, $t_{23} = \alpha t_{22}$ ($\alpha = 0 \sim 2$), $U = U' + 2J_H$. The Hilbert space of the two-site three-orbital model is comprised of 495 states, we exactly diagonalize the Hubbard Hamiltonian as shown Eq.(S.8) to obtain the four lowest energy levels, the three lowest energy levels of which correspond to total spin angular momentum $S=0,1,2$. Here, we set $t_{22} = 0.3$ eV, $\Delta = 0.5$ eV, $U = 5$ eV, $J_H = U/5$, which is similar with previous reference [18]. As shown in **FIG. S9**, we plot the four lowest energy levels vs t_{23}/t_{22} . From the three lowest energy levels, we can extract J and K according to $J = (E_2 - E_1)/2$, and $K = E_0/3 + E_2/6 - E_1/2$. The magnitudes of J and K as the function of t_{23}/t_{22} are also shown in the **FIG. S9(a)**. We can see that J changes from antiferromagnetic coupling to ferromagnetic coupling with the increase of t_{23}/t_{22} , whereas K is always negative and changes slightly. The calculated ratio of

bilinear and biquadratic exchange interaction β ($-K/J$) as function of t_{23}/t_{22} with the typical parameters is also shown in **FIG. S9** (b). Obviously, $\beta(-K/J)$ diverges at $t_{23}/t_{22} \sim 1$, which means that J changes from antiferromagnetic coupling to ferromagnetic coupling when t_{23}/t_{22} crossovers the critical value ~ 1 . At this stage, we test another three sets of parameters to observe whether different hopping amplitude affect the qualitative conclusion. All the results are plotted in **FIG. S10**, **FIG. S11** and **FIG. S12**. Based on the results shown in **FIG. S10**, **FIG. S11** and **FIG. S12**, it is found that β diverges when t_{23}/t_{22} approaches a specific value, thus the qualitative conclusion remains unchanged.

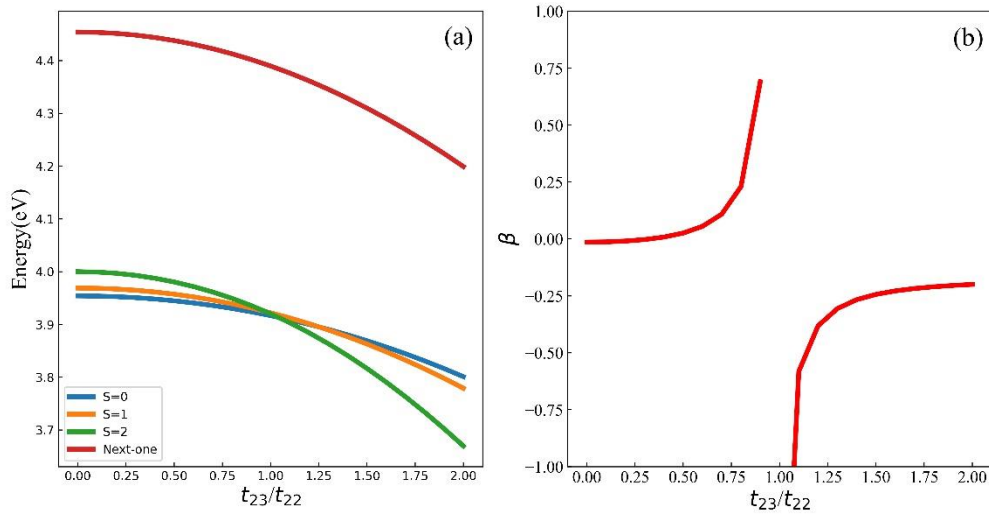


FIG. S9 (a) Four lowest energy levels with chosen parameters ($t_{11} = t_{12} = t_{13} = t_{33} = 0$, $t_{22} = 0.3$ eV, $\Delta = 0.5$ eV, $U = 5$ eV, $J_H = U/5$). Note the large gap between the lowest energy levels (blue line: $S = 0$; orange line: $S = 1$; green line: $S = 2$) and the highest energy level (red line). (b) The ratio of biquadratic and bilinear interaction β ($-K/J$) as function of t_{23}/t_{22} .

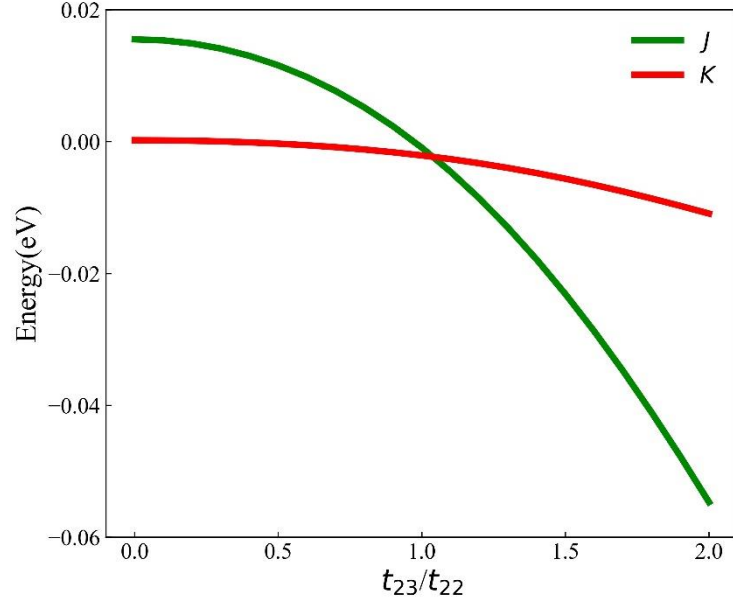


FIG. S10 J (NN bilinear exchange interaction) and K (NN biquadratic exchange interaction) extracted from the lowest energies E_S levels with the parameters as **FIG. S5**.

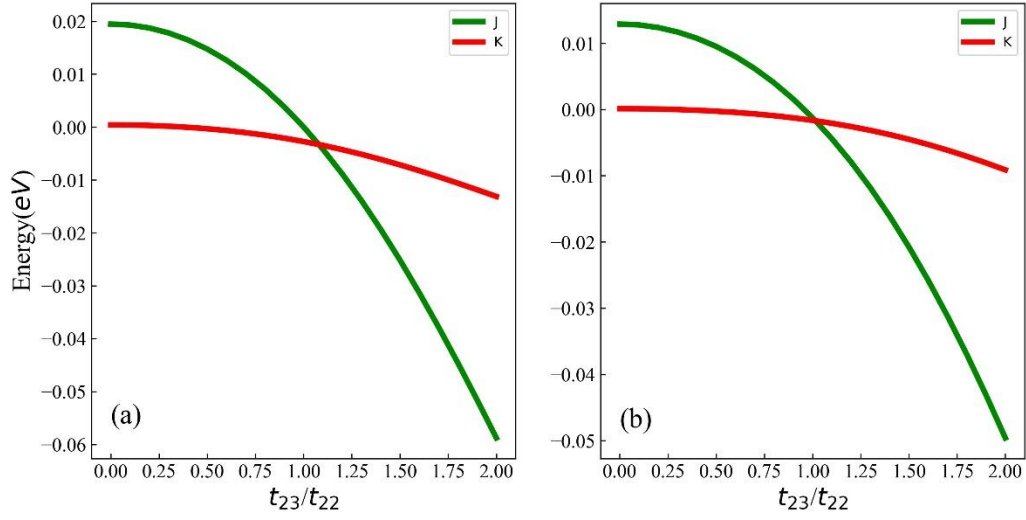


FIG. S11 J and K with different U values (Δ fixed with 0.3 eV, $t_{11} = t_{12} = t_{13} = t_{33} = 0$, $t_{22} = 0.3$ eV) for (a) $U = 4$ eV. (b) $U = 6$ eV.

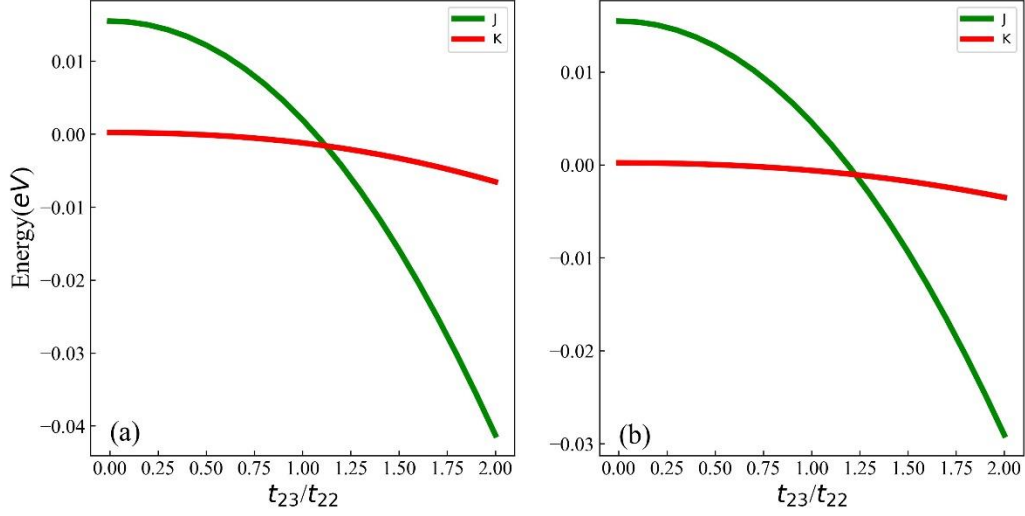


FIG. S12 J and K with different crystal field splitting Δ (U fixed with 5 eV, $t_{11} = t_{12} = t_{13} = t_{33} = 0$, $t_{22} = 0.3$ eV). (a) $\Delta = 0.7$ eV. (b) $\Delta = 1.0$ eV.

To see the role of the empty orbital, we consider two-site two orbitals Hubbard model, in which one site provides two orbitals occupied by two electrons. Similar as the above three-orbital model, we set $t_{11} = t_{22}$, $t_{12} = t_{21}$, $U = U' + 2J_H$ and $\Delta \ll U'$, J_H . The Hilbert space is composed of 70 states with different spin angular moments. Within this Hilbert space, we diagonalize the Hubbard Hamiltonian and extract the bilinear and biquadratic exchange parameters. In our calculation, we adopt $t_{11} = 0.3$ eV, $U = 5$ eV, $J_H = U/5$, which are same as the case of **FIG. S9**. We plot four lowest energy levels in **FIG. S13**, from which we find that there exists a large gap between the highest energy level and three lowest energy levels and three lowest energy levels do not cross in the interval $[0, 2]$. Thus, the two-site two orbitals model has a different conclusion, that is, bilinear exchange interaction J is always AFM and biquadratic exchange interaction K is always close to zero in the chosen region of $t_{12}/t_{11} [0, 2]$. Combining two-site two-orbital model with two-site three-orbital model, we can conclude that the hopping from occupied orbital to empty orbital ($\sim t_{23}$) has a decisive role on the origin of giant biquadratic exchange interaction K .

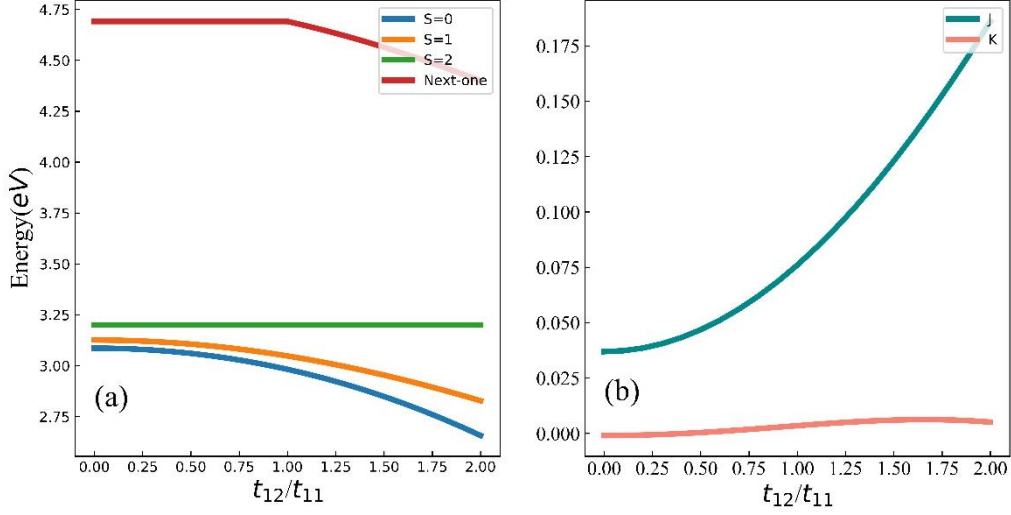


FIG. S13 (a) Four lowest energy levels of two-orbital Hubbard model. (b) J and K extracted from three lowest energies E_S levels.

3 Effective hopping interactions in NiX₂

In the second part of Section III, we analyze the origin of giant biquadratic exchange interaction K based on the two-site Hubbard model. Now we turn to our case, NiX₂. Since the Ni ion is surrounded by X ion forming octahedron, there are two hopping processes, i.e., direct and indirect hopping. Here we consider the indirect hopping Ni-X-Ni since the direct hopping between two Ni ions is usually small. The indirect hopping can be viewed as effective hopping through perturbative techniques.

In the following derivation, the different geometry of bond is considered. For the case of 180° Ni-X-Ni as shown in **FIG. S14**, the Slater-Koster (SK) integrals [19] for p - and d -orbitals are divided into two parts: from left- d -orbital to p -orbital and from p -orbitals to right- d -orbital. The SK integrals for hopping from left- d -orbital to p -orbital and from p -orbital to right- d -orbital are listed in the **Table S4** and **Table S5**. As for the case of 90° Ni-X-Ni as shown in **FIG. S15**, the SK integrals for hopping from left d -orbital to p -orbital are same with the 180° Ni-X-Ni, while the SK integrals for hopping from left d -orbital to p -orbital are different, which are listed in the **Table S6**.

Table S4 The SK integrals for hopping from left- d -orbital to p -orbital and from p -orbital to right- d -orbital.

	d_{xy}	d_{yz}	d_{zx}	$d_{x^2-y^2}$	d_{z^2}
p_x	0	0	0	$-\frac{\sqrt{3}}{2}V_{pd\sigma}$	$\frac{1}{2}V_{pd\sigma}$
p_y	$-V_{pd\pi}$	0	0	0	0
p_z	0	$-V_{pd\pi}$	0	0	0

Table S5 The SK integrals for hopping from left- d -orbital to p -orbital and from p -orbital to right d -orbital.

	d_{xy}	d_{yz}	d_{zx}	$d_{x^2-y^2}$	d_{z^2}
p_x	0	0	0	$\frac{\sqrt{3}}{2}V_{pd\sigma}$	$-\frac{1}{2}V_{pd\sigma}$
p_y	$V_{pd\pi}$	0	0	0	0
p_z	0	$V_{pd\pi}$	0	0	0

Table S6 The SK integrals for hopping from the p -orbital to right d -orbital in the case of 90° geometry.

	d_{xy}	d_{yz}	d_{zx}	$d_{x^2-y^2}$	d_{z^2}
p_x	$V_{pd\pi}$	0	0	0	0
p_y	0	0	0	$\frac{\sqrt{3}}{2}V_{pd\sigma}$	$-\frac{1}{2}V_{pd\sigma}$
p_z	0	$V_{pd\pi}$	0	0	0

As we can see from the **Table S4** and **Table S5**, the possible hopping channels for the case of 180° Ni-X-Ni are:

- (1) $d_{xy} \rightarrow p_y \rightarrow d_{xy}, \Rightarrow t_{dd} = \frac{-(V_{pd\pi})^2}{\Delta}$
- (2) $d_{x^2-y^2} \rightarrow p_x \rightarrow d_{x^2-y^2}, \Rightarrow t_{dd} = \frac{-3(V_{pd\sigma})^2}{4\Delta}$
- (3) $d_{z^2} \rightarrow p_x \rightarrow d_{z^2}, \Rightarrow t_{dd} = \frac{-(V_{pd\sigma})^2}{4\Delta}$
- (4) $d_{x^2-y^2} \rightarrow p_x \rightarrow d_{z^2}, \Rightarrow t_{dd} = \frac{\sqrt{3}(V_{pd\sigma})^2}{4\Delta}$
- (5) $d_{z^2} \rightarrow p_x \rightarrow d_{x^2-y^2}, \Rightarrow t_{dd} = \frac{\sqrt{3}(V_{pd\sigma})^2}{4\Delta}$

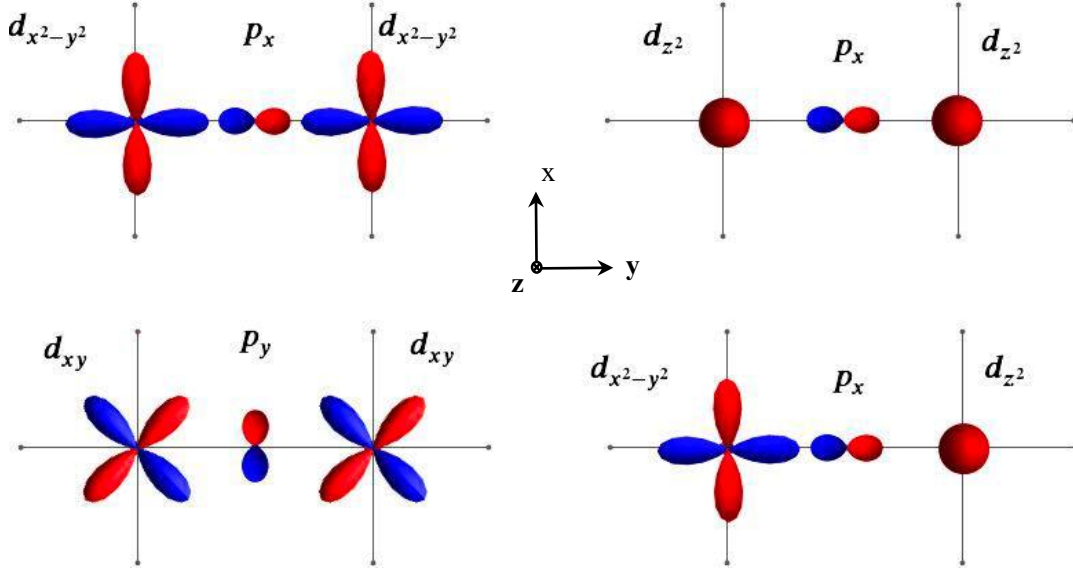


FIG. S14 Possible hopping channels for the case of 180° Ni-X-Ni. Blue and red lobes represent the positive and negative charge density, respectively.

As we can see from the **Table S6**, the possible hopping channels for the case of 90° Ni-X-Ni are:

- (1) $d_{xy} \rightarrow p_y \rightarrow d_{x^2-y^2}, \Rightarrow t_{dd} = - \frac{\sqrt{3}V_{pd\sigma}V_{pd\pi}}{2\Delta}$
- (2) $d_{x^2-y^2} \rightarrow p_x \rightarrow d_{xy}, \Rightarrow t_{dd} = - \frac{\sqrt{3}V_{pd\sigma}V_{pd\pi}}{2\Delta}$
- (3) $d_{z^2} \rightarrow p_x \rightarrow d_{xy}, \Rightarrow t_{dd} = - \frac{V_{pd\sigma}V_{pd\pi}}{2\Delta}$
- (4) $d_{xy} \rightarrow p_y \rightarrow d_{z^2}, \Rightarrow t_{dd} = - \frac{V_{pd\sigma}V_{pd\pi}}{2\Delta}$

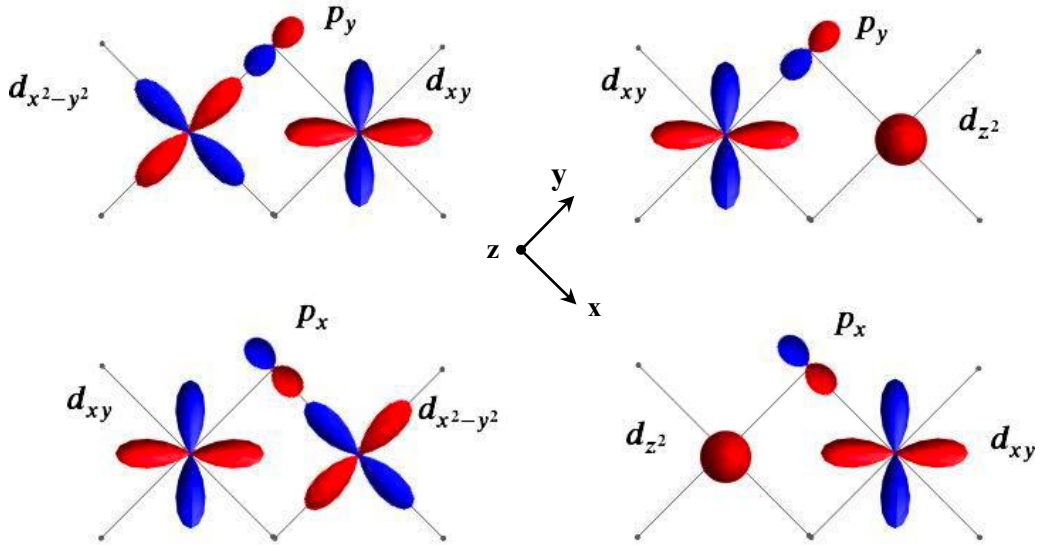


FIG. S15 Possible hopping channels for the case of 90° Ni-X-Ni. Blue and red lobes represent the positive

and negative charge density, respectively.

Here, t_{dd} stands for the effective hopping from left d -orbital to right d -orbital, which is estimated from the second-order perturbation theory, and $\Delta = U + \Delta_{pd}$, where U is coulomb repulsion energy and $\Delta_{pd} = \varepsilon_d - \varepsilon_p$ is the transfer gap.

Obviously, there are five hopping channels in the case of 180° Ni-X-Ni, which include hopping terms in the e_g manifold ($(d_{x^2-y^2}, d_{x^2-y^2})$, $(d_{z^2} - d_{z^2})$, $(d_{x^2-y^2}, d_{z^2})$) and t_{2g} manifold (d_{xy} - d_{xy}). Therefore, the hopping occurs between the e_g and e_g orbitals, t_{2g} and t_{2g} orbitals, while the hopping between the t_{2g} and e_g orbitals are absent (diagonal and off-diagonal hopping). In contrast to the case of 180° Ni-X-Ni, the hopping can only occur between t_{2g} and e_g orbitals in the case of 90° Ni-X-Ni. As stated in main text, “1” and “2” represent the e_g orbitals and “3” denotes as t_{2g} orbitals, the ratio of hopping from e_g to t_{2g} and hopping from e_g to e_g ($\alpha = t_{23}/t_{22}$) is zero in the case of 180° Ni-X-Ni, while α is gigantic for the case of 90° Ni-X-Ni.

Above, we discuss two specific geometries, in real materials, the bond deviates from these two geometries. Below, let us see how α changes with the bond angle of TM-ligand-TM. The hopping from left- d_{z^2} to right- d_{z^2} (t_{22}) can be written in the function of θ (see main text):

$$t_{22}(\theta) = -V_{pd\sigma} \cos[\theta] (1/4 * V_{pd\sigma} (\cos[\theta]^2 + \sin[\theta]^2)) \quad (\text{S.10})$$

Similarly, the hopping integrals between left- d_{xy} and right d_{z^2} (t_{23}) can be written in the function of θ :

$$t_{23}(\theta) = 1/2 * V_{pd\pi} V_{pd\sigma} \sin[\theta] (\cos[\theta]^2 + \sin[\theta]^2) \quad (\text{S.11})$$

Therefore, $\alpha = \frac{t_{23}}{t_{22}} = -2 * (\frac{V_{pd\pi}}{V_{pd\sigma}} \tan[\theta])$. Here, we set $\frac{V_{pd\pi}}{V_{pd\sigma}} \sim 1/10$, so that

$$\alpha = \frac{t_{23}}{t_{22}} = -1/5 \tan[\theta] \quad (\text{S.12})$$

For 180° Ni-X-Ni, the ratio α is closed to zero, which corresponds to small β ($-K/J$), and for 90° Ni-X-Ni the ratio α approaches infinite, corresponding to large β ($-K/J$). Hence, in the edged shared octahedron, the biquadratic exchange is strong.

Section IV. Biquadratic exchange interactions in monolayer CrCl_3 , CrI_3 , CrGeSe_3 and CrSiTe_3

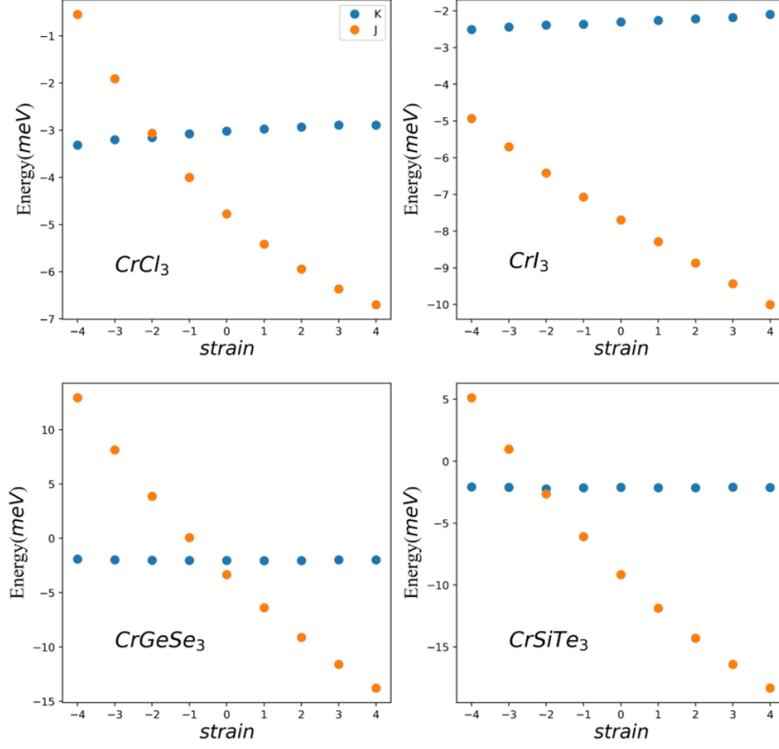


FIG. S16 The nearest neighbor bilinear and biquadratic exchange interaction of monolayer CrCl_3 , CrI_3 , CrGeSe_3 and CrSiTe_3 as the function of strain. Yellow dots represent nearest neighbor Heisenberg exchange J , while blue dots denote biquadratic exchange K of nearest neighbor pairs. The nearest neighbor exchange J changes with strain linearly, whereas the nearest neighbor biquadratic exchange K almost remain invariant.

Section V. Additional results on fictitious perovskite NaNiCl_3

For the fictitious perovskite NaNiCl_3 , we extract bilinear exchange parameter J and biquadratic exchange parameter K based on the four-state method. In **FIG. S17**, we plot the ratio of K/J . We find that the magnitude of the ratio increases with the decrease of bond angle (in the range from 180° to 120°), which is consistent with our TB analysis.

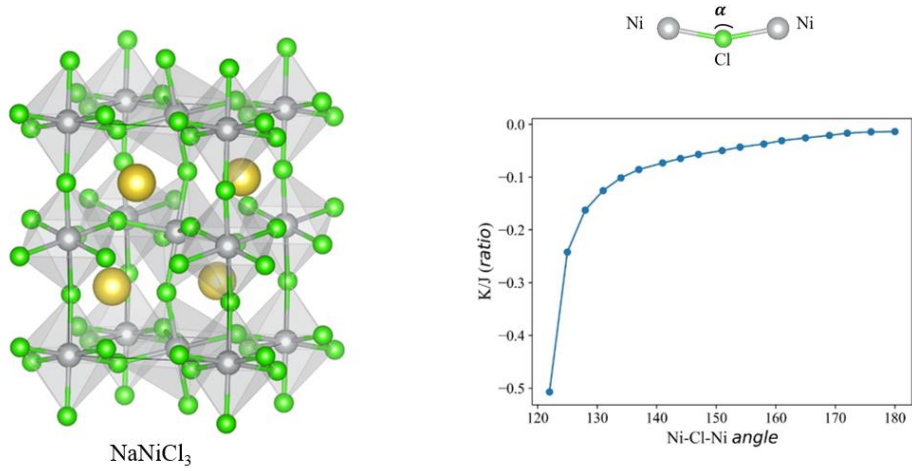


FIG. S17 Crystal structure of fictitious perovskite NaNiCl₃ (left panel) and K/J vs bond angle (right panel).

- [1] P. E. Blochl, Phys. Rev. B **50**, 17953 (1994).
- [2] G. Kresse and J. Furthmüller, Phys. Rev. B **50**, 17953 (1996).
- [3] J. P. Perdew, K. Burke, and M. Ernzerhof, Phys. Rev. Lett. **77**, 3865 (1996).
- [4] A. I. Liechtenstein, V. V. Anisimov, and J. Zaanen, Phys. Rev. B **52**, R5467 (1995).
- [5] M. McGuire, Crystals **7**, 121 (2017).
- [6] H. J. Xiang, E. J. Kan, S.-H. Wei, M. H. Whangbo, and X. G. Gong, Phys. Rev. B **84**, 224429 (2011).
- [7] H. Xiang, C. Lee, H. J. Koo, X. Gong, and M. H. Whangbo, Dalton Trans. **42**, 823 (2013).
- [8] X. Li, F. Lou, X. Gong, and H. Xiang, New J. Phys. **22**, 053036 (2020).
- [9] P. S. Wang and H. J. Xiang, Phys. Rev. X **4**, 011035 (2014).
- [10] K. Hukushima and K. Nemoto, J. Phys. Soc. Jpn. **65**, 1604 (1996).
- [11] A. I. Liechtenstein, M. I. Katsnelson, V. P. Antropov, and V. A. Gubanov, J. Magn. Magn. Mater. **67**, 65 (1987).
- [12] A. A. Mostofi, J. R. Yates, Y.-S. Lee, I. Souza, D. Vanderbilt, and N. Marzari, Comput. Phys. Commun. **178**, 685 (2008).
- [13] G. Pizzi *et al.*, J. Phys. Condens. Matter. **32**, 165902 (2020).
- [14] X. He, N. Helbig, M. J. Verstraete, and E. Bousquet, Comput. Phys. Commun. **264** (2021).

- [15] O. Besbes, S. Nikolaev, N. Meskini, and I. Solovyev, Phys. Rev. B **99**, 104432 (2019).
- [16] I. V. Solovyev, Phys. Rev. B **103**, 104428 (2021).
- [17] M. J. Freiser, Phys. Rev. **123**, 2003 (1961).
- [18] F. Mila and F. C. Zhang, Eur. Phys. J. B **16**, 7 (2000).
- [19] J. C. Slater and G. F. Koster, Phys. Rev. **94**, 6 (1954).